Pacific Equatorial Subsurface Countercurrent Velocity, Transport, and Potential Vorticity*

G. DAIL ROWE AND ERIC FIRING

University of Hawaii at Manoa, Honolulu, Hawaii

GREGORY C. JOHNSON

NOAA/Pacific Marine Environmental Laboratory, Seattle, Washington

(Manuscript received 27 January 1999, in final form 22 June 1999)

ABSTRACT

Concurrent shipboard ADCP and CTD sections are used to calculate the mean velocity, transport, and potential vorticity fields associated with the Pacific equatorial subsurface countercurrents (SCCs). Averaged in stream coordinates, the core eastward velocity of the SCCs is a factor of 2 higher than previously reported means, but the estimated transports are unchanged. The meridional profile of zonal velocity along isopycnals is sharply peaked, and nearly linear on each flank of the current. The sharp and strong reversal of relative vorticity over a distance of 20 km at the jet core sharpens the coincident potential vorticity front. This front separates a region of very low homogeneous potential vorticity on the equatorward side from a homogeneous high potential vorticity region on the poleward side. Each potential vorticity pool extends well beyond the edges of the SCC into regions of westward flow. On the equatorward sides of the SCCs this westward flow is the Equatorial Intermediate Current in the western Pacific, but in the central and eastern parts of the basin it is off the equator in deep extensions of the South Equatorial Current. In the central and eastern regions the net westward transport in an isopycnal layer between the SCCs exceeds the combined eastward SCC transport in that layer. The net zonal transport between the SCC cores is highly divergent in the east and convergent in the west. This pattern, together with downstream changes in SCC density, indicates that neither they nor the westward return flows are simple inertial recirculations; strong diapycnal processes must be involved.

1. Introduction

The subsurface countercurrents (SCCs, also known as Tsuchiya jets) in the Pacific (Tsuchiya 1975) are narrow eastward currents that bracket the equator just below the equatorial thermocline (Fig. 1). They form the poleward boundaries of the 13°C equatorial thermostad. The northern SCC (NSCC) begins west of 141°E at 325-m depth, and the southern SCC (SSCC) begins near 155°E, just to the east of New Ireland, at 300-m depth (Fig. 2). Both SCCs start 3° from the equator, then gradually diverge and shoal to the east until they are 6° from the equator and 150 m below the surface at 110°W. The SCCs have a typical core speed of 35 cm s^{-1}, and transport 5–10 Sv each (Sv $\equiv 10^6$ m^3 s^{-1}).

The SCCs were first described in detail by Tsuchiya (1975), based on several meridional hydrographic sections in the eastern tropical Pacific. [See Tsuchiya (1975) for the history of SCC observations prior to 1975.] Hayes et al. (1983), analyzing nine hydrographic sections along 110°W, confirmed Tsuchiya's observation of the remarkable steadiness of the NSCC in the eastern Pacific; no sign of an annual cycle was found. In the central Pacific, Wyrtki and Kilonsky (1984) showed the geostrophic currents relative to 1000 dbar based on the mean of about 30 sections made during one year along 158°W, 153°W, and 150°W. (Only the 10 sections along 150°W extended south of 4°S.) Unsurprisingly, the SCC velocities were weaker in this mean than in individual sections, while their transports were still substantial: 8.9 Sv in the NSCC and 4.3 Sv in the SSCC. Interestingly, two SSCC branches were shown, the main one centered at 4°S, 250 m, and a weaker one at 7°S, 320 m. Tsuchiya (1975) also notes the existence of a weak but consistent eastward countercurrent south of the SSCC in the eastern Pacific. We will refer to the latter as the ''secondary

* University of Hawaii School of Ocean and Earth Science and Technology Contribution Number 5008; University of Hawaii Joint Institute for Marine and Atmospheric Research Contribution Number 00-331; Pacific Marine Environmental Laboratory Contribution Number 2052.

Corresponding author address: Dr. G. Dail Rowe, Accurate Environmental Forecasting, 165 Dean Knauss Rd., Narragansett, RI 02882.
E-mail: drowe@accufore.com

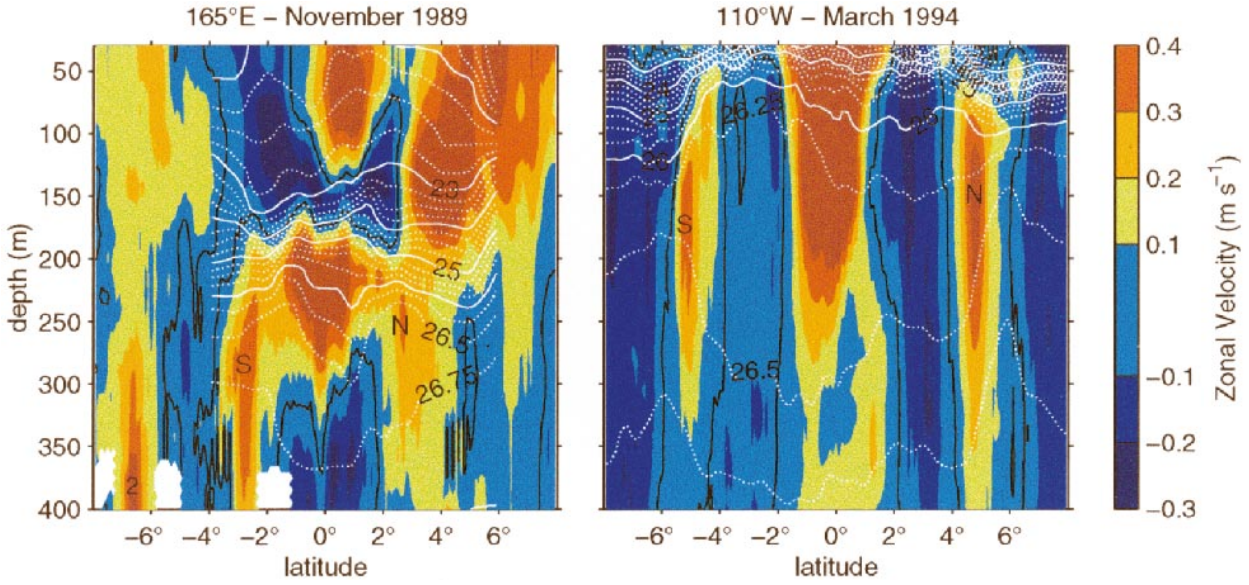

FIG. 1. Typical synoptic sections of zonal velocity and neutral density showing the SCCs in the western Pacific (left) and in the eastern Pacific (right). At 165°E the SCCs (labeled S for the SSCC and N for the NSCC) usually appear as distinct velocity maxima embedded in eastward flow connected to both the Equatorial Undercurrent and the North Equatorial Countercurrent. As the SCCs flow eastward, they rise with the equatorial thermocline, diverge from the equator, and become distinct eastward jets embedded in a westward background flow. The secondary SSCC (labeled 2) is apparent in the 165°E section. The zero zonal velocity contour is black, integer neutral density contours are solid white, and 0.25 kg m^{-3} contours are dotted white.

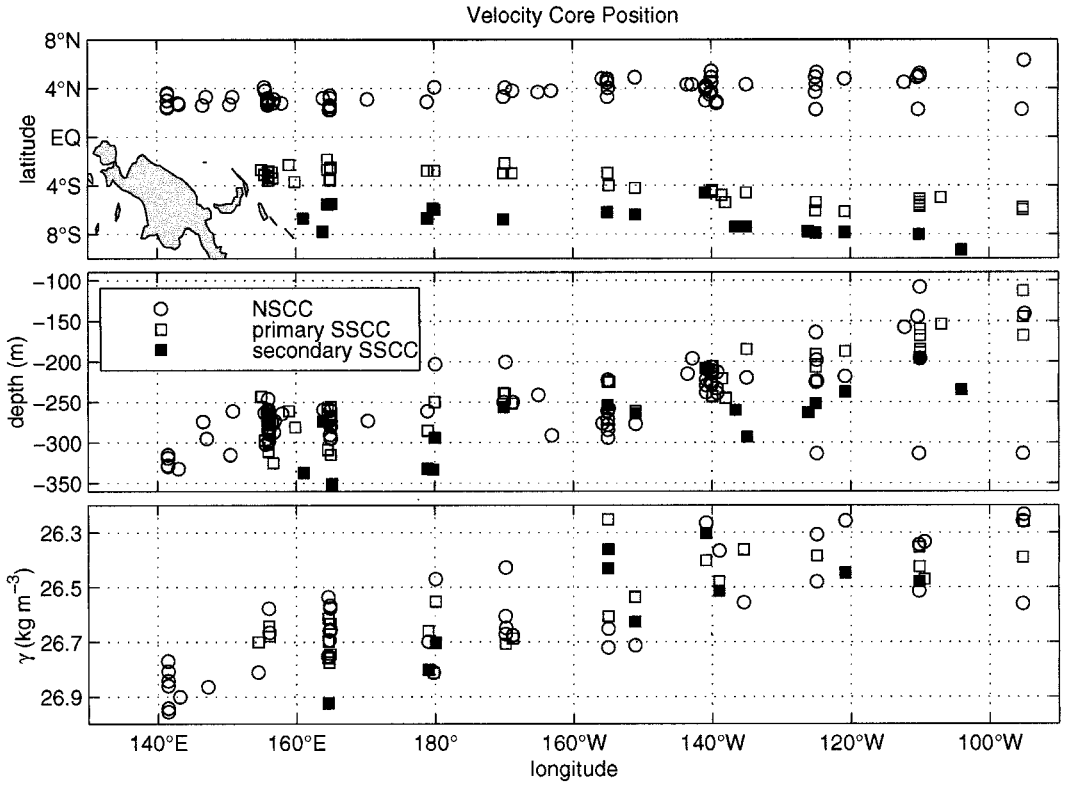

FIG. 2. Core positions of the SCCs. The SCCs diverge from the equator, rise with the equatorial thermocline, and become progressively lighter as they flow eastward. A secondary eastward jet poleward of the primary SSCC is occasionally observed at 165°W, and consistenty observed by the dateline.

SSCC'' and use ''SSCC'' with no modifier to designate the main branch.

Unlike all other studies of the SCCs to date, the western Pacific data analysis by Gouriou and Toole (1993) included direct velocity measurements as well as CTD profiles. They compiled mean sections on 165°E, 142°E, and 137°E, averaging properties on density surfaces. The SCCs appear as symmetric lobes of the Equatorial Undercurrent (EUC) in their mean zonal velocity section on 165°E. Unlike the EUC, the SCC transports showed no sign of annual variation in separate summer and winter averages. On 142°E there is no SSCC because the region south of the equator is within the Bismarck Sea, but the NSCC appears again as a lobe of the EUC. No direct velocity measurements were available on 137°E. In the geostrophic velocity section there is no minimum between the North Equatorial Countercurrent (NECC) and the deeper eastward flow in the NSCC density range, so Gouriou and Toole chose to combine the latter into the NECC. This deeper flow occurs at 3°N, the same latitude as the NSCC on 142°E, so we believe that it should be labeled NSCC on 137°E as well.

Including the meridional derivative of zonal velocity in their calculation of potential vorticity (PV) on density surfaces, Gouriou and Toole (1993) noted that the SCCs coincide with fronts separating regions of uniformly low PV on the equatorward side from higher values on the poleward side. The NSCC PV front is also a salinity front [see also Johnson and McPhaden (1999)]. They suggested that the low PV and relatively uniform salinity between the SCCs might indicate that an equatorial intermediate current (EIC) recirculates part of the SCC waters. On a larger scale, Tsuchiya (1981) identified the SSCC and the deeper part of the EUC as the last parts of the circuitous isopycnal path to the thermostad in the eastern equatorial Pacific for water formed in the Tasman Sea. In contrast, Toggweiler et al. (1991) suggested that the thermostad water originated as subantarctic mode water and gradually moved upward across isopycnals; in this view, diapycnal mixing plays a dominant role.

Recently, Johnson and Moore (1997) and Johnson and McPhaden (1999) have comprehensively described the SCCs based on all available hydrographic data in the tropical Pacific, averaged on density surfaces and objectively mapped with 1° resolution in latitude. Johnson and Moore show that the observed downstream divergence from the equator, shoaling, and narrowing of the SCCs are consistent with an inertial model. They noted that the downstream decrease in density, however, is not explained by the model, indicating that diapycnal diffusion is another important factor in SCC dynamics. Johnson and McPhaden (1999) emphasize the basinwide PV front in the core of each SCC, and suggest that the part of each SCC poleward of its front is the equatorward limb of a recirculation gyre in which the westward return flow is relatively broad and weak. They do not discuss recirculation equatorward of the PV front, probably because the small dynamic height gradients near the equator do not rise above the noise.

The inertial model of Johnson and Moore (1997) is consistent with many aspects of SCC downstream variation, but does not specify their forcing mechanism. McPhaden (1984) proposed a linear, vertically diffusive model that developed weak SCCs as lobes of the EUC. The model weakly resembles observations in the western Pacific but not in the central or eastern Pacific where the actual SCCs are well separated from the EUC. Numerical models, with the notable recent exception of a global high-resolution ocean general circulation model (Ishida et al. 1998), have failed to develop SCCs in the Pacific. Analogous currents in the Atlantic, however, have been described observationally (e.g., Tsuchiya 1986; Mayer et al. 1998) and in a numerical model (Schott and Böning 1991).

In the present study, high-resolution direct velocity measurements are combined with concurrent hydrographic sections to sharpen the description of the SCCs. Velocity sections from shipboard acoustic Doppler profilers (SADCP) have now sampled the SCCs across most of the Pacific, often with 10-km effective horizontal resolution. We preserve most of this resolution by using minimal smoothing and by averaging on isopycnals in stream coordinates, centered on the SCC core latitude in each section. The resulting peak mean velocities are larger than earlier estimates, and the PV front at the core of each SCC is of roughly 40-km width, considerably smaller than previously reported (Gouriou and Toole 1993). Following Johnson and McPhaden (1999), we view the PV fronts as likely transport streamlines, and we then use our velocity measurements to estimate the basinwide isopycnal transport balance at SCC densities in the entire equatorial zone between the fronts. It appears that diapycnal mass flux must be a major factor in the transport balance.

2. Data and methods

Most of the SADCP data used in this study are available from the U.S. National Oceanographic Data Center (NODC) via its Joint Archive for Shipboard ADCP (JASADCP; available online at http://ilikai.soest.hawaii.edu/sadcp) at the University of Hawaii. Of the 220 cruises archived at the JASADCP at the commencement of this study, 44 have measurements of Pacific SCCs. These 44 cruises contain 170 crossings of individual SCCs: 93 of the NSCC and 77 of the SSCC. Hydrographic measurements accompany the SCC velocity sections on 29 of the cruises. Major contributing programs include the World Ocean Circulation Experiment (WOCE), the United States/People's Republic of China (US/PRC) cooperative program for Air–Sea Interaction, the Coupled Ocean–Atmosphere Response Experiment (COARE), and the ongoing Tropical Atmosphere Ocean (TAO: McPhaden et al. 1998) buoy array maintenance cruises of the NOAA Ship *Ka'imimoana.*

Given the diversity of data sources and the evolution of technology during the 12 years of observations, as well as the natural range of sea conditions, the quality of the SADCP data is inevitably variable and impossible to characterize with a single number. Biases exceeding 10 cm s^{-1} may occur in parts of some of the earlier datasets, but 5 cm s^{-1} is probably a better estimate of the typical errors averaged over 50 km or so. The dominant error source is the transducer orientation; when underway at 6 m s^{-1}, a 0.5° compass error causes 5-cm-s^{-1} error in the cross-track velocity component. Starting in about 1992, most cruises have had the benefit of GPS based heading estimates which reduce heading errors, and the associated cross-track velocity errors, by an order of magnitude (King and Cooper 1993). Even for the earlier cruises, however, we believe that for the purposes of this study the SADCP errors are unimportant; they are mostly smaller, and no more systematic, than the high-frequency ocean current variability that we view as noise in the present study. The depth range of the SADCP data, however, is a major limitation in this study. It is especially a problem in the western Pacific, where the SCCs are deepest and where ADCP depth range tends to be poorer than in the east. (High productivity due to equatorial upwelling in the eastern equatorial Pacific supports a large biomass, and acoustic backscattering is correspondingly high.) Under ideal conditions the SADCP range exceeds 400 m, but lack of scatterers or rough weather sometimes cuts the range to 200 m or less; overall, 300 m is typical.

Although the SADCP data are typically recorded, processed, and archived with 5-min temporal resolution, corresponding to 1.8 km alongtrack for 6 m s^{-1} cruising speed, the effective resolution is less; noise in the navigation measurements, and hence in estimates of the ship's velocity over the ground, requires smoothing of the raw estimates of current over the ground. The earliest cruises were heavily smoothed so that their effective resolution is little better than 0.5° of latitude, but the majority of the cruises have effective resolution of 10 km. In the vertical, nominal 8-m sample spacing is most common. For the present analysis we regridded all SADCP sections to integer multiples of 10 m in the vertical and 0.1° in latitude. CTD profiles were used to correct the depths for the difference between nominal and true sound speed.

We calculate the velocity structure, transport, and PV of the SCCs in 0.1 and 0.2 kg m^{-3} layers centered on neutral densities, γ, (Jackett and McDougall 1997) ranging from 26 to 27 kg m^{-3}. Neutral density values calculated on the original pressure and latitude grid were linearly interpolated to an even 0.1° latitude × 2-decibar pressure grid. Gaps larger than 1.1° were not filled. The positions of neutral surfaces were then estimated, and the velocity of each neutral layer was calculated as the depth-averaged velocity between the neutral surfaces. Latitudinal SCC boundaries were estimated for individual neutral layers using the transition from positive to negative mean neutral-layer velocity as the jet boundary when possible; otherwise, a subjective estimate of the latitude of an appropriate local velocity minimum was used. (For example, in the western Pacific the upper part of each SCC usually blends into the EUC, and the NSCC sometimes blends into the NECC, as in the 165°E section of Fig. 1.) Transport estimates for each neutral layer were calculated as the meridional integral of the product of mean neutral-layer velocity and neutral-layer thickness. The meridional shear was estimated using the centered finite difference approximation

$$\frac{\partial u}{\partial y} = \frac{u_{n+1} - u_{n-1}}{2\Delta y} \tag{1}$$

after the individual mean neutral-layer velocities were meridionally smoothed with a 3-point Hanning filter. PV was estimated as

$$\frac{f - \partial u/\partial y}{h}. \tag{2}$$

The meridional velocity field in the vicinity of the SCCs is dominated by waves, which effectively mask any meridional velocity signal associated with the SCCs in both synoptic and mean measurements. We believe that neglecting the presumably small contribution of $\partial v/\partial x$ has not significantly contaminated our PV estimates. Note that the neutral layer thickness h was meridionally smoothed in the same manner as the velocity field. The underlying resolution of h however, is usually 0.5°–1°, much coarser than that of velocity. This implies that the 40-km width of the SCC PV front is likely an upper bound, but the CTD station spacing has less effect on the meridional structure of our PV estimates than one might initially expect. Because of the geostrophic balance, thickness varies as the meridional integral of the vertical shear. Small-scale structure in PV is therefore dominated by the more highly differentiated term, the horizontal shear, rather than thickness. In the discussion below, it is sometimes useful to discuss the contribution of relative vorticity to the PV. For this purpose, the term ''relative PV,''

$$\frac{-\partial u/\partial y}{h}, \tag{3}$$

will be used.

All quantities are calculated for individual sections, and the sections are averaged in stream coordinates centered on each SCC velocity core. (The term ''core'' will normally be used for the location of the velocity maximum, either of the entire current or within a specified depth or density range. The modifier ''transport'' will be used to indicate the maximum in transport per unit width for a given density interval, or the density range of maximum transport per unit density increment.) The core latitude was chosen subjectively by inspection of the layer-averaged zonal velocity as a function of latitude. Usually the local maximum was obvious, partic-

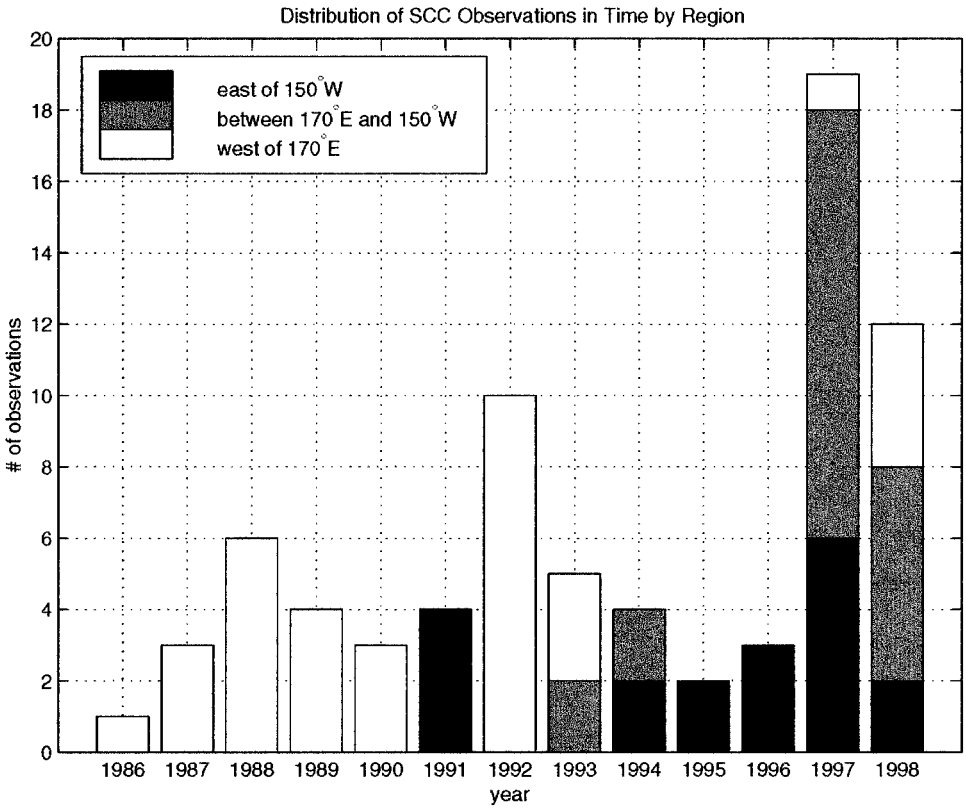

FIG. 3. Distribution in time and region of SCC observations with both velocity and density data.

ularly for the layers of strongest flow. Sometimes a single maximum had to be chosen from two neighboring roughly equal maxima, and, particularly in the lighter layers in the western Pacific, the SCC sometimes merged into the EUC without a clear SCC maximum; in these cases, a point was chosen consistent with the bulk of the current at all levels. The core latitude was allowed to shift gradually with density, but no more than 30-km difference from top to bottom was permitted.

Sections are averaged in three longitude bins: west of 170°E (western Pacific), between 170°E and 150°W (central Pacific), and east of 150°W (eastern Pacific). Nonuniform sampling in time and latitude adversely affects the averages in two ways. First, observations in the western Pacific are dominated by data from the late 1980s (US/PRC) and early 1990s (COARE), while the central and eastern Pacific data are dominated by more recent measurements (TAO; see Fig. 3). Associated with the El Niño–Southern Oscillation (ENSO) cycle are highly variable currents near the equator, and there is no guarantee that El Niño, La Niña, and ''normal'' years have all been sampled uniformly in any of the three regions. Hence, some of what we describe as longitudinal variability may actually be temporal. Second, some sections did not span the entire 5° width over which stream coordinate averaging was performed [see panels (a) and (d) of Figs. 4, 5, and 6]. This distribution can lead to jumps in plots of properties as a function of latitude. We do not believe that either of these sampling problems obscures the basic structure of the SCCs.

We have chosen to use the largest dataset available for each analysis. For showing core positions as functions of latitude and depth, for example, we do not need CTD measurements, so more samples are available than for the plot of core position as a function of density (Fig. 2). Meridionally integrated transport calculations sometimes have fewer samples than meridional profiles because they require gap-free CTD and SADCP sections spanning the limits of integration. Quantities calculated for deep layers have fewer samples than for shallow layers because of the limited SADCP depth range.

3. SCC description

The description of SCC structure is organized in five parts. First, the core positions from all individual transects are discussed. Groups of transects are then averaged in stream coordinates and as a function of density to show the mean velocity, potential vorticity, and then transport. Finally, the velocity structure of the secondary SSCC is described.

a. Core position

The core positions determined from SADCP sections (Fig. 2 and Table 1) show the well-known eastward

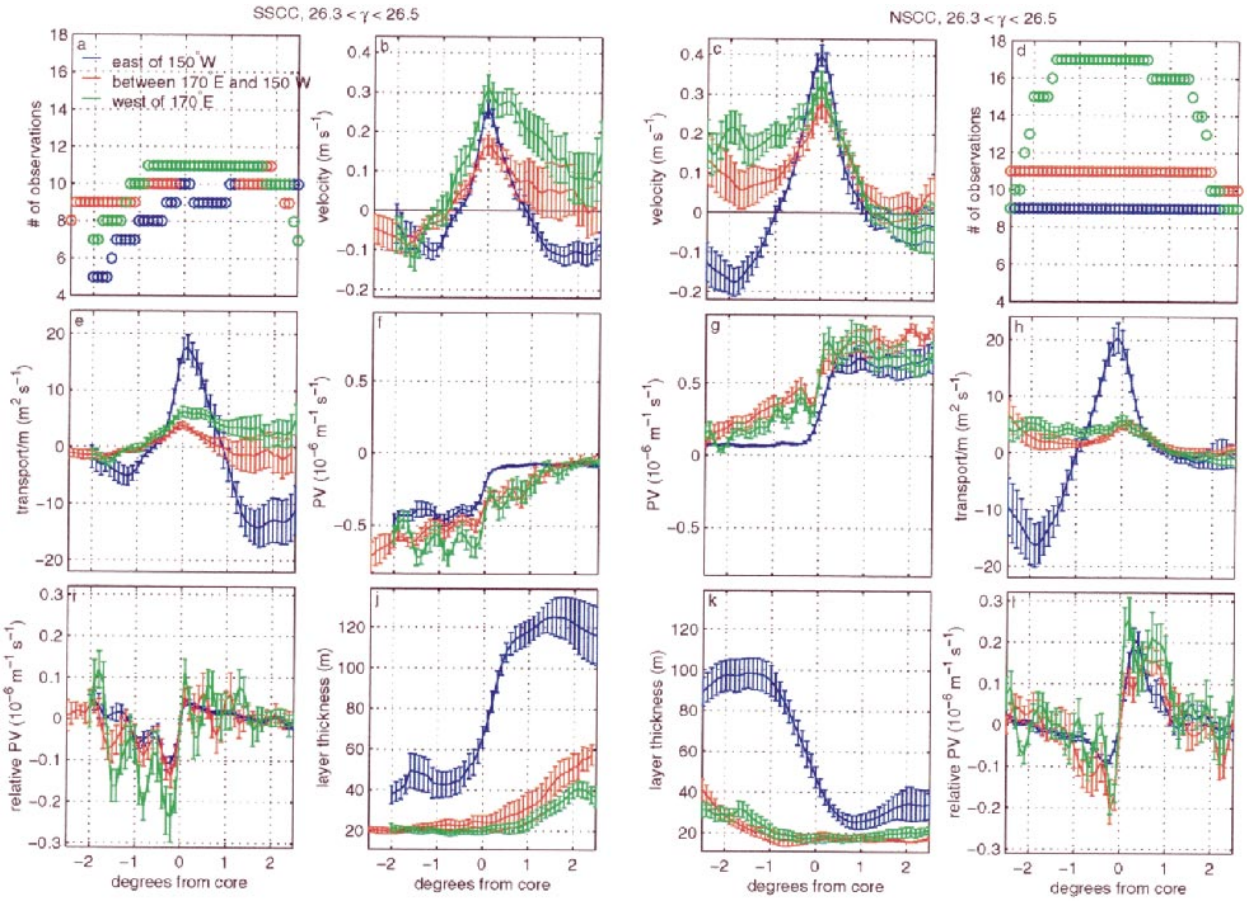

FIG. 4. SCC properties in the 26.3–26.5 kg m^{-3} neutral density layer, averaged in three longitude ranges. The abcissa in all panels is degrees latitude from the current core, positive to the north. Panels are arranged symmetrically about the equator in the middle; NSCC quantities are on the right half, SSCC on the left. Fewer observations were available in the south (a) than in the north (d). Layer-averaged velocity [(b) and (c)] shows that the SCCs in the eastern Pacific are isolated eastward flows, while the central and western Pacific SCCs are slight extrema in an eastward flow connected to the EUC. Potential vorticity [(f) and (g)] is low on the equatorward side of each SCC and rises sharply at the velocity maximum to uniformly high values on the poleward side; only in the east is it homogeneous on the equatorward side, however. Layer thickness [(j) and (k)] is larger on the equatorward side of each SCC; the pycnostad is well developed in the east. Relative PV [(i) and (l)] sharpens the PV front at each SCC core. The error bars show one standard error.

shoaling and divergence from the equator of the SCCs. The NSCC and SSCC begin in the far western Pacific about 3° from the equator and 300 m below the surface. Shoaling and divergence from the equator appear to start near 170°E. By 125°W the SCCs have reached their maximum open-ocean latitude of about 6°, but they continue shoaling to a minimum depth near 150 m at 95°W. In our easternmost section, 88°W (not shown or used in any calculation in this paper), a possible SSCC branch is found at 9.5°S, but an NSCC core is not apparent. Evidently the SCCs lose their character as strong zonal jets somewhere between 95° and 88°W, 500 km or more from the eastern boundary.

The density of the SCC cores appears to decrease almost linearly with longitude all the way from the westernmost observations at 141°E to about 140°W, east of which density remains constant while the depth continues to decrease (Fig. 2). The NSCC has a core γ of about 26.85 kg m^{-3} at 141°E. The westernmost SSCC sections, at 155°E, show a core γ of about 26.7 kg m^{-3}. Both SCC cores lighten at about 0.1 kg m^{-3} per 20° longitude until they reach approximately 26.4 kg m^{-3} at 140°W. The core densities are similar to the pycnostad densities which lighten to the east (Johnson and Moore 1997).

Temporal variability in SCC core positions is evident in Fig. 2. Although the focus of this paper is on the mean, some aspects of the temporal variability are relevant as indicators of the representativeness of our mean picture. A sample of short-term variability in the western Pacific is provided by the cluster of sections near 156°E, nearly all of which were collected during the approximately 3-month intensive observation period of COARE. During this time both SCCs underwent meridional excursions of about 1.5° peak to peak and depth variations within a 100-m range. A longer time period was sampled by the seven cruises of the US/PRC program along 165°E between November 1986 and July

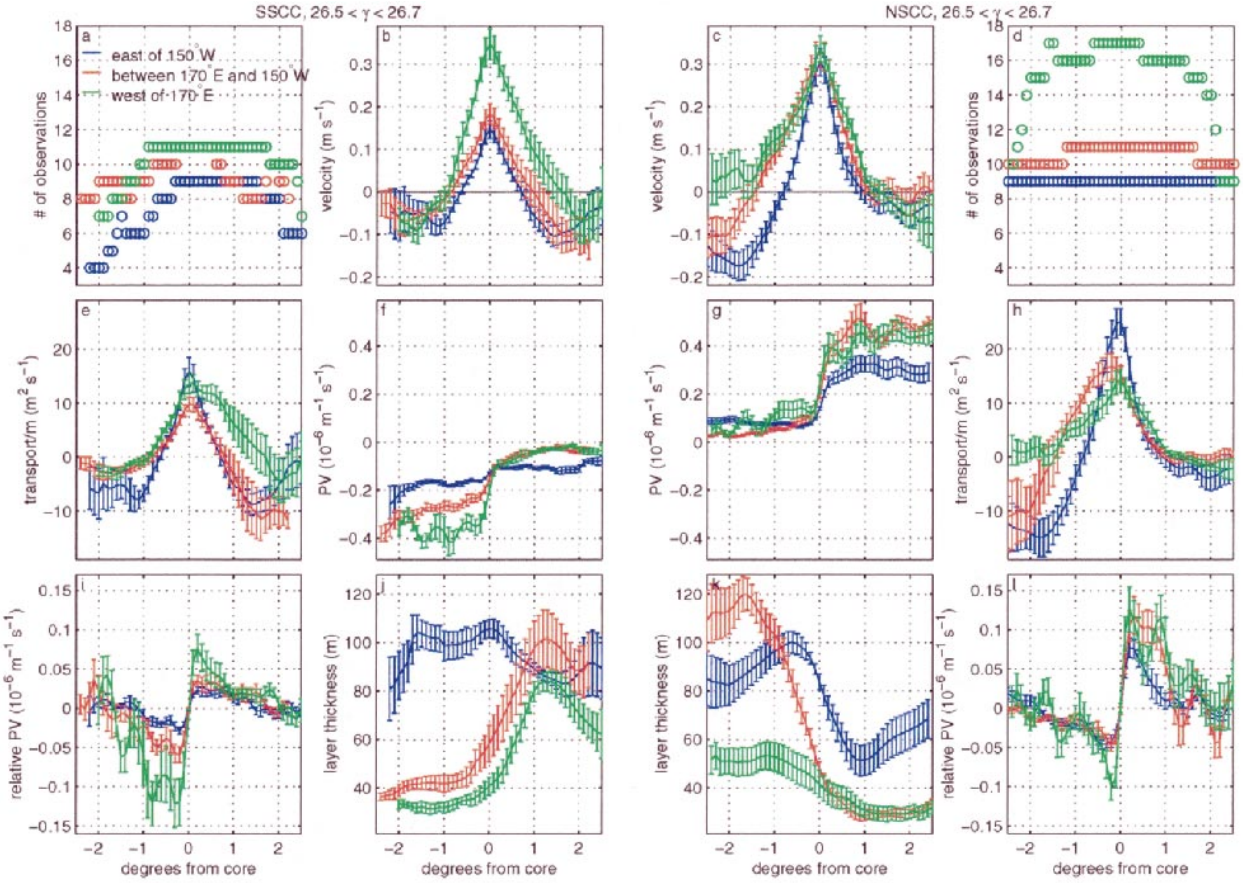

FIG. 5. SCC properties in the 26.5–26.7 kg m^{-3} neutral density layer, shown as in Fig. 4. Central and eastern SCCs are isolated eastward flows with westward flow on the equatorward side (b, c). In this density class the pycnostad extends across most of the Pacific (j, k), and all SCCs except the eastern SSCC have a substantial PV front at their core (f, g).

1990. SCC core positions from this set of sections are no more variable than those from the 3-month COARE period on 156°E, indicating that there is not a large seasonal or interannual signal in western Pacific SCC position. The eastern Pacific sections clustered near 140°W, however, show NSCC cores in a 3° range, twice the range in the western Pacific. The growth in SCC position variability with longitude is also evident in the standard deviation of SCC core position shown in Table 1: eastern Pacific SCC core position variability is approximately three times that found in the west. Meridional shifts on 140°W occur over intraseaonal and longer timescales. In particular, preliminary analysis of this dataset suggests that tropical instability waves drive intraseasonal variability of the NSCC and that the SCCs migrate meridionally with annual periodicity. A closer look at the temporal variability of the SCCs is planned for the near future.

b. *Velocity structure*

Meridional profiles of velocity in neutral density layers reveal a number of interesting features: high maximum speed, triangular shape, westward flows on the flanks, a weaker SSCC in the central and eastern regions, and consistent core structure as the SCCs lighten to the east [panels (b) and (c) in Figs. 4, 5, and 6]. The density of the SCC velocity cores is near 26.75 kg m^{-3} in the western Pacific, 26.6 kg m^{-3} in the central Pacific, and 26.4 kg m^{-3} in the eastern Pacific (Fig. 2). Thus, Fig. 4 (26.3–26.5 kg m^{-3}) represents the eastern Pacific SCC cores, Fig. 5 (26.5–26.7 kg m^{-3}) represents the central Pacific SCC cores, and Fig. 6 (26.6–26.8 kg m^{-3}) represents the structure in and slightly above the western SCC cores; the depth range of the ADCP dataset does not permit us to center the density range on the actual core density in the west.

The mean core speeds of the SCCs, 35–40 cm s^{-1} for the NSCC and the western SSCC and 18–20 cm s^{-1} for the central and eastern SSCC, are about a factor of 2 higher than reported in previous studies using averaged observations (Johnson and Moore 1997; Gouriou and Toole 1993; Wyrtki and Kilonsky 1984; Tsuchiya 1975), but consistent with high resolution synoptic geostrophic estimates for the eastern NSCC (Hayes et al. 1983). Some of this difference is clearly due to the coarse

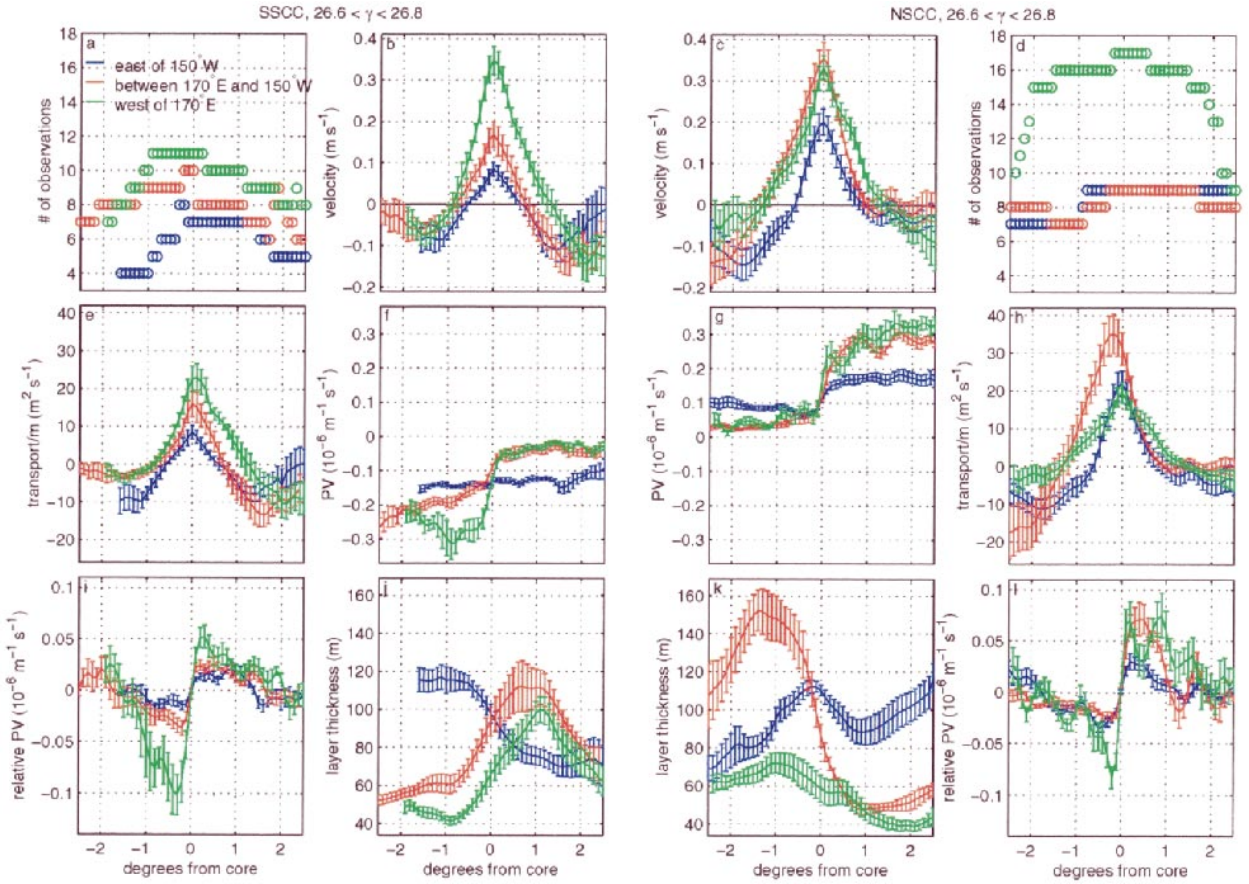

FIG. 6. SCC properties in the 26.6–26.8 kg m^{-3} neutral density layer, shown as in Fig. 4. The western and central SCCs retain much of their essential character in this density class, but the eastern SCCs are greatly diminished (b, c). Note that the pycnostad has shifted to the poleward side of the SCCs in the eastern region (j, k).

horizontal resolution of geostrophic velocity estimates which typically represent velocity averaged over 50–100-km intervals; our SADCP averaging interval is 10 km. However, given the 1.5°–3° range of temporal variability in core latitude and the 2° total width of the currents, stream-coordinate averaging yields a mean that typifies the synoptic observations; averaging in fixed latitude coordinates does not (Fig. 7). The SSCC velocity profiles in the central and eastern regions are slower by a factor of 2, and narrower, compared to the western region; they are also slower than the corresponding NSCC profiles in the central and eastern regions. This may be related to the existence of the secondary SSCC described in section 3e.

The nearly triangular shape of the SCC core velocity profile is even more striking than the maximum speed; but the sharpness of the peak, and the magnitude of the curvature at the velocity maximum, are actually *underestimated* in Figs. 4, 5, and 6. After our 10-km averaging and 3-point Hanning smoothing, a perfectly triangular profile becomes indistinguishable from the observed profiles in regions and density layers with core speeds exceeding 30 cm s^{-1}.

Both SCC cores are flanked by westward flows of 10–20 cm s^{-1} on their equatorward sides in all three longitude bins. In the western Pacific the westward flow is the EIC, filling the latitude range between the NSCC and the SSCC. In the eastern Pacific the eastward flow of the EUC extends down through the SCC density range, and the westward flows on the equatorward flanks of the SCCs might be described as lobes of the South Equatorial Current (SEC; see Fig. 1). The strongest of the equatorward flanking currents in Figs. 4, 5, and 6 is north of the equator in the eastern Pacific.

We attempted to estimate the mean meridional-velocity field and its divergence using the same techniques applied to the zonal component, but no robust patterns could be identified. The strong meridional-velocity fluctuations due to equatorial waves and eddies obscure

TABLE 1. The mean and standard deviation of SCC velocity core latitude in the western, central, and eastern regions.

	West	Central	East
NSCC	2.9 ± 0.4	4.1 ± 0.7	4.1 ± 1.1
SSCC	−3.0 ± 0.4	−3.1 ± 0.7	−5.7 ± 1.3

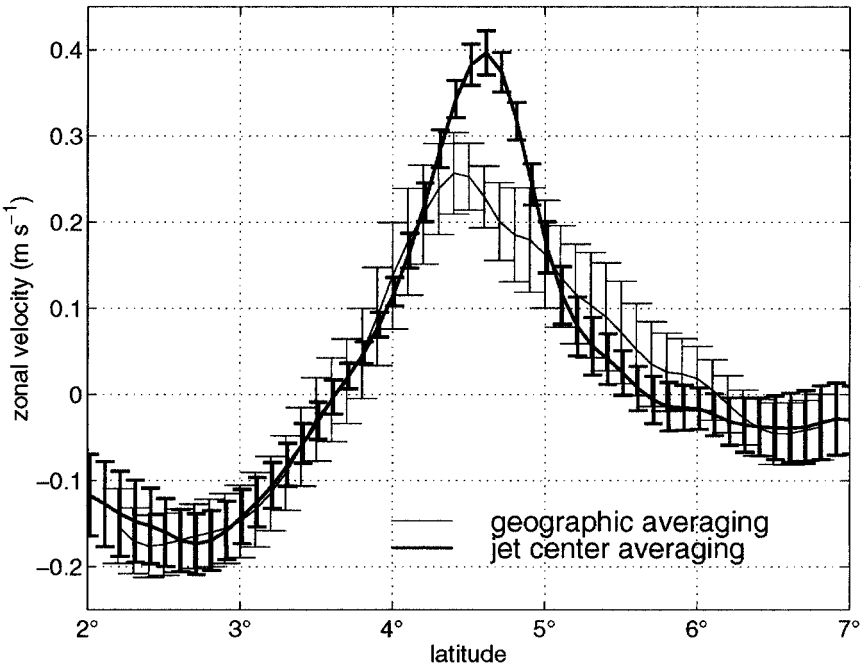

FIG. 7. Zonal component of current in the NSCC averaged vertically over the 26.3–26.5 kg m^{-3} neutral density layer. The nine sections east of 150°W are averaged in geographical coordinates (light line) and in stream coordinates (heavy line). The latter emphasizes the narrowness and speed of the NSCC as seen in synoptic sections. The stream coordinate profile is aligned with its core at the mean latitude of the individual section cores.

whatever weak meridional velocity component may be associated with the SCCs. A preliminary look at recent sections on 95°W that are not included in the present analysis indicates that the NSCC has a consistent northward component there, near its terminus as a recognizable current. This issue will be revisited in future work as the available dataset grows.

c. Potential vorticity

In both the NSCC and the SSCC, and in all three regions, the potential vorticity in a neutral density layer is almost a step function of distance from the SCC core, particularly in the layer containing the velocity peak for each region [panels (f) and (g) of Figs. 4 for the eastern region, Fig. 5 for the central region, and Fig. 6 for the western region]. The PV gradient at the front is dominated by the reversal in sign of the shear term, $\partial u/\partial y$, which we are estimating using centered differences (hence dy of 20 km) of a smoothed velocity field [panels (i) and (l) of Figs. 4, 5, and 6]; hence the PV gradient is underestimated in this analysis. Both poleward and equatorward of the front at the SCC core density, in regions extending well beyond the transition from eastward to westward flow, PV appears to be constant in latitude within two standard errors, with one exception. On the equatorward side in the western and central regions there is a gradual decrease in PV magnitude toward the equator. This trend is more pronounced in the shallowest layer (above the core) in the western and central regions. Nevertheless, we will refer to the regions of nearly constant PV as PV pools; compared to the PV jump at the front, changes in PV between each SCC flank and its adjacent region of zero or westward flow are small.

In the east, the densest layer is effectively below the SSCC. The PV jump, weak in the middle layer in this region, is absent in the densest layer, where PV is nearly constant across the jet and the peak speed is only 8 cm s^{-1}. The eastern SSCC may be weak in this layer because the secondary SSCC tends to transport the denser water in the southeast (sec. 3e).

The nearly step-function PV structure of the SCCs (two homogenous PV pools separated by a front 40 km wide) is caused by both the h and the shear term in (2). Isopycnals spread equatorward in an eastward jet, so the equatorward decrease in f is augmented by an increase in h; PV decreases more rapidly than it would if h were constant. Relative vorticity magnifies the effect at the core and reduces it on the flanks; in the Northern Hemisphere, relative vorticity switches from positive on the north side of the jet to negative on the south side. It is this rapid reversal of relative PV that makes the PV front in the SCCs so sharp [Fig. 8 and panels (i) and (l) in Figs. 4, 5, and 6]. Without the shear term, the PV gradient is increased by the h term throughout an eastward jet, not just at its core. Conversely, both the shear and the h term weaken the PV gradient in west-

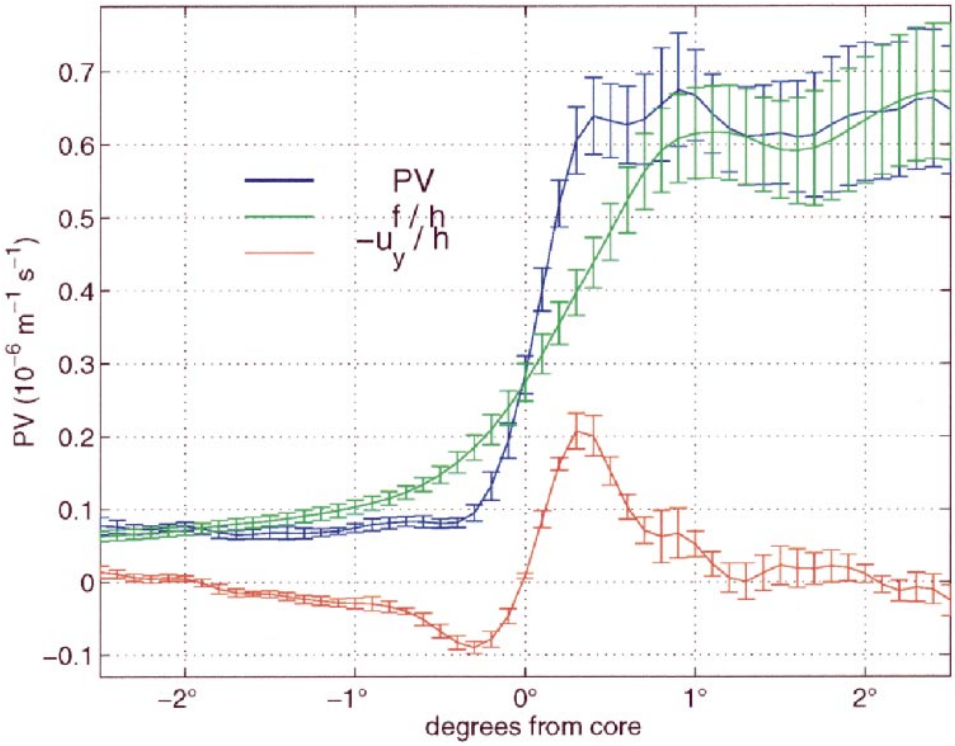

FIG. 8. NSCC core potential vorticity components for the layer 26.3–26.5 kg m^{-3} east of 150°W. The relative PV term (red) is smaller than the planetary PV (green), but it is significant in sharpening the potential vorticity front at the NSCC core (blue). As in Fig. 7, the 26.3–26.5 kg m^{-3} neutral density layer is averaged over the nine sections east of 150°W.

ward jets. Increased property gradients in eastward jets, and decreased gradients in westward jets, have been noted by Gouriou and Toole (1993).

Potential vorticity varies with longitude on both sides of the SCC cores primarily between the central and eastern regions. The predominant tendency in all three density layers on the poleward sides of the fronts, and in the lightest layer on the equatorward sides, is for PV to decrease in magnitude to the east; in these regions, the increase in layer thickness to the east more than compensates for the increase in f as the SCCs diverge from the equator. The opposite trend is seen in the two deeper layers on the equatorward sides: there the magnitude of PV increases from the central to the eastern region. PV is relatively uniform from the western to the central region except on the poleward side of the SSCC.

d. Transport

Large spatial variations in layer thickness are related to the distribution of SCC transport as a function of latitude, density, and region. As a function of latitude, the transport curve in neutral density layers [panels (e) and (h) in Figs. 4–6] is generally skewed toward the equator relative to the velocity [panels (b) and (c)in Figs. 4–6]; this is particularly clear in the lightest layer of the eastern region (Fig. 4) and the two deeper layers of the central region in the Northern Hemisphere. These are the places where the equatorward increase in layer thickness [panels (j) and (k) in Figs. 4–6] is largest.

The large increase in thickness of the shallowest layer, 26.3–26.5 kg m^{-3}, from the central to the eastern region corresponds to a large transport increase; although the velocity profiles in Fig. 4 show only fractional differences in peak velocity among the regions, the transport profiles show large SCC transports in the eastern region and little in the other regions. This layer thickness is 95–120 m on the equatorward sides of the SCCs in the east versus 30–60 m in the central and western regions.

Plotting total SCC transport as a function of density in 0.1 kg m^{-3} layers emphasizes the downstream decrease in density of the transport core (Fig. 9). The NSCC core starts in the west at or below the deepest density bin, 26.9 kg m^{-3}, and rises to 26.7 kg m^{-3} in the central region and to 26.5 kg m^{-3} in the east. The downstream rise in the transport core is larger and more consistent than the corresponding rise in transport-weighted neutral density calculated by Johnson and Moore (1997, their Table 1). This discrepancy likely reflects the difference between the mean of the potential density transport and the mode of potential density transport, the differences in datasets, and/or the differences in range of integration in Johnson and Moore (1997) versus the present study. The SSCC profile in the west is similar to the corresponding NSCC, at least down to 26.7 kg m^{-3}, which appears to be the transport

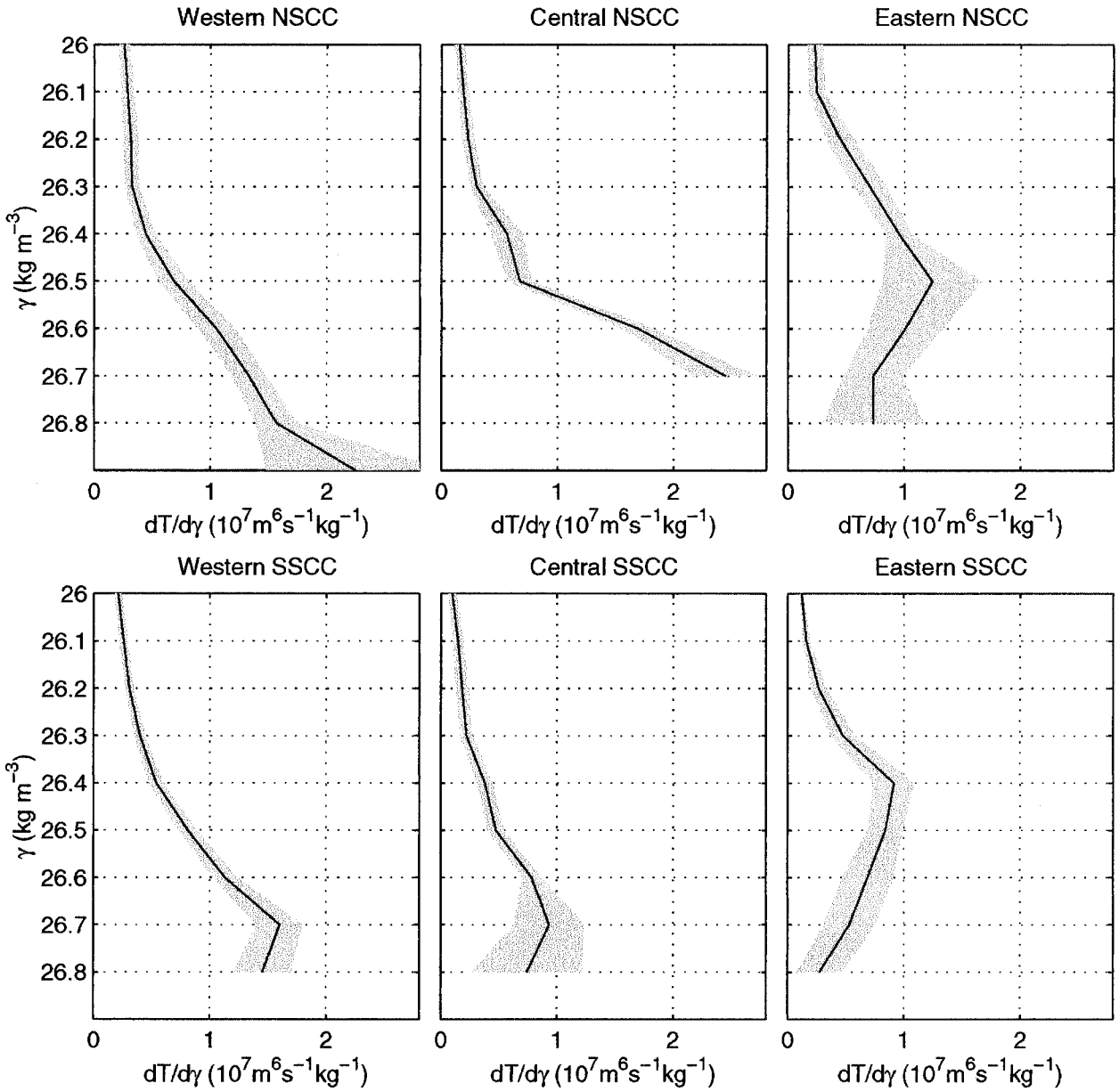

FIG. 9. NSCC (top row) and SSCC (bottom row) transport per unit potential density. Transports were calculated in isopycnal layers 0.1 kg m^{-3} thick centered on γ values between 26 and 27 kg m^{-3}. SCC transport cores progressively lighten as the currents flow across the Pacific. The shading represents one standard error. Three or more samples were available for each point.

core in the south. The central SSCC profile is much weaker than the western SSCC or the central NSCC. The eastern SSCC reaches its peak at 26.4 kg m^{-3}; overall, its transport is at lower densities than the eastern NSCC. Adding the transport of the secondary SSCC (sec. 3e) to that of the main SSCC (Fig. 10) shifts the net transport to greater densities in the central region; we expect it would have the same effect in the east, although we lack sufficient observations of the secondary SSCC there to verify this hypothesis.

Particularly in the western and central regions, the SADCP measurements do not extend deep enough to sample the entire SCCs; nevertheless, in Table 2 we compare the transport within SADCP range to prior estimates of total SSC transport. As expected, our NSCC estimate in the west is low; but in the western SSCC and the central NSCC and SSCC, our estimates are surprisingly close to prior estimates. Either the latter are also underestimates or the fraction of total transport that we are missing is small. Our eastern SSCC estimate is only 60% of that of Johnson and Moore (1997) at 110°W. The reason is not clear, but may be related to the larger longitude range covered by our average. Considering our transport estimates as lower bounds, to-

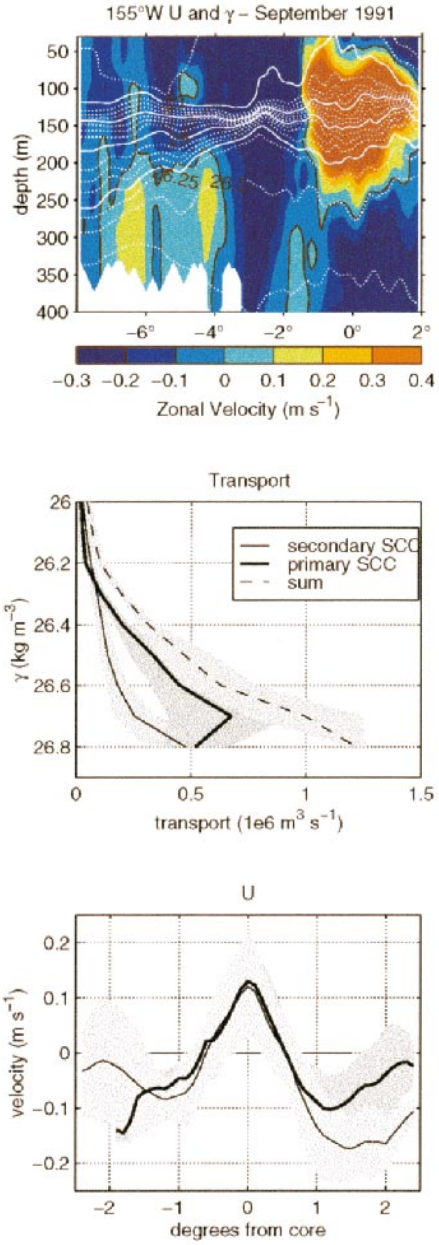

FIG. 10. Secondary SSCC compared to the primary SSCC Top panel zonal velocity and neutral density along 155°W; the secondary SSCC is centered near 6.5°S and the primary SSCC is at 4°S. The zero zonal velocity contour is black, integer neutral density contours are solid white, and 0.25 kg m^{-3} contours are dotted white. Middle and bottom panels: stream-coordinate comparisons of the transport and velocity structure of the two SSCCs for the six transects with high quality ADCP and CTD observations of both SSCCs. Longitudes range from 180°–140°W. The secondary SSCC transports denser water than the primary SSCC but has similar velocity structure.

gether with the prior estimates, it is apparent that both the NSCC and the SSCC lose 25%–50% of their transport between the western and central regions. There is no clear change between the central and eastern regions. Transport estimates in the west may be higher partly because of the ambiguity in defining the SCCs there: they are usually connected to the EUC, and the NSCC is often connected to the NECC.

TABLE 2. Total SCC transport in Sv, within the depth range of the SADCP, compared to prior estimates of total SCC transport.

	NSCC	SSCC
Western	7.8 ± 0.9	6.9 ± 0.5
	10.3[a]	6.6[a]
	11.7[b]	7.6[b]
	14.8[c]	8.8[c]
Central	7.5 ± 0.7	3.4 ± 0.4
	7.0[a]	4.1[a]
	7.7[d]	4.3[d]
Eastern	6.1 ± 1.3	3.9 ± 0.6
	7.4[a]	6.2[a]
	8[e]	4[e]

[a] Johnson and Moore (1997).
[b] Gouriou and Toole (1993).
[c] Delcroix et al. (1987).
[d] Wyrtki and Kilonsky (1984).
[e] Tsuchiya (1975).

e. The secondary SSCC

A second subthermocline eastward current was often observed 1° or 2° south of the primary SSCC; for example, see Fig. 10 and the 165°E section in Fig. 1. This secondary SSCC was almost always found between 180° and 120°W on sections that went far enough south, but was only sporadically seen outside that longitude band. The primary and secondary SSCC velocities have nearly identical meridional structure relative to their cores (Fig. 10), but the secondary core is deeper and denser (Fig. 2). Within the range of the SADCP, the secondary SSCC transport was about 60% of the primary SSCC transport.

It is not clear whether the secondary SSCC is an independent current flowing continuously from the western to eastern Pacific or whether it splits from the primary SSCC somewhere in the west, perhaps at a time-varying longitude. Observations of the secondary SSCC as far west as 160°E argue for an independent origin, but the sporadic nature of the secondary SSCC in the western Pacific combined with the drop in transport and peak velocity of the SSCC between the western and central Pacific makes the bifurcation hypothesis attractive. An extensive subsurface float dataset might be required to settle the issue.

4. Circulation

The observed downstream changes in SCC density and transport show that the SCCs cannot be regarded simply as pipes carrying water from the western boundary to the eastern; there must be isopycnal recirculation and/or diapycnal mass flux along the way. Transport as a function of latitude in the layer 26.3–26.5 kg m^{-3} [panels (e) and (h) in Fig. 4] suggests isopycnal recir-

TABLE 3. Transport in Sv for the SCCs and equatorward flows in the neutral density layer 26.5–26.6 kg m^{-3}. SCC transports are separated into the portions poleward and equatorward of the current core (PV front). For purposes here, the EIC is defined as all flow between the equatorward edges of the SCCs. For these calculations, only sections with continuous density and velocity coverage were used, leaving seven samples in the west, six in the central region, and four in the east. Results were similar for the shallower layer 26.4–26.5 kg m^{-3}; the calculation could not be done for deeper layers because of gaps in the ADCP coverage. The limited number of samples makes robust statistical statements impossible; in particular, the EIC transports in the central and eastern Pacific are not statistically different.

	Western	Central	Eastern
Poleward of NSCC core	0.6 ± 0.1	0.4 ± 0.1	0.6 ± 0.2
Equatorward of NSCC core	0.7 ± 0.1	0.5 ± 0.1	1.0 ± 0.2
Total NSCC	1.3 ± 0.3	0.9 ± 0.2	1.5 ± 0.3
EIC	−0.4 ± 0.9	−3.2 ± 1.2	−4.9 ± 2.6
Equatorward of SSCC core	0.6 ± 0.2	0.3 ± 0.1	0.5 ± 0.3
Poleward of SSCC core	0.4 ± 0.1	0.2 ± 0.1	0.3 ± 0.1
Total SSCC	1.0 ± 0.2	0.4 ± 0.1	0.8 ± 0.3
EIC + Equatorward portion of SCCs	0.9 ± 0.9	−2.4 ± 1.2	−3.4 ± 2.9
EIC + all SCCs	1.9 ± 0.9	−1.9 ± 1.2	−2.5 ± 2.9

culation; in the east, the strong SCCs are flanked on their equatorward sides by at least equally strong westward flows, but in the central and western regions the adjacent westward transports are small. Poleward flow from the westward currents into the SCCs may be occurring between eastern and central regions in this layer.

To quantify the isopycnal circulation balance, we calculate transports for the layer 26.5–26.6 kg m^{-3}, which is within the SCCs all across the basin. Meridional boundaries are at the poleward edge of each SCC, at each SCC core, and at the equatorward edge of each SCC. The net transport between the equatorward edges of the SCCs is labeled ''EIC'' for convenience, even though in the eastern and central regions it includes eastward EUC transport and westward flow connected to the SEC. The SCC transports are calculated separately for each side of the PV front; as noted by Gouriou and Toole (1993) and Johnson and McPhaden (1999), the fronts are likely to be streamlines.

The largest flows in this layer (Table 3) are not for the SCCs but for the EIC; in the east, its westward transport, 4.9 Sv, overwhelms the 1.5 Sv combined eastward transport of the SCCs equatorward of their PV fronts, and even the 2.3-Sv total SCC transport. There is a *net westward* transport between the SCC fronts mounting to 3.4 Sv in the eastern region and 2.4 Sv in the central region. The net in the western region is weakly eastward, 0.9 Sv. The uncertainties are large, but the pattern is clear. Between the eastern boundary and the eastern region, there is a large flux into the layer: a diapycnal convergence and/or eastern boundary inflow from higher latitudes. Between the eastern and western regions there is at least as large a flux out of the layer. If the PV fronts are indeed streamlines, then this interior flux out of the layer *must be diapycnal.* The weak eastward net flow in the western region is consistent with a net input from the western boundary as suggested by Tsuchiya (1981). The strong inflow into the eastern region is most likely diapycnal; the tracer fields and acceleration potential presented by Tsuchiya (1975) and Johnson and McPhaden (1999) suggest that the meridional flow along the coast of South America in the SCC density range is poleward rather than equatorward.

Presently available evidence therefore suggests a circulation for the central SCC layer, 26.5–26.6 kg m^{-3}, as drawn in Fig. 11. The SCC cores, diverging from the equator as the SCCs flow eastward, are boundaries between recirculation gyres. The poleward gyre of the NSCC has been discussed by Johnson and McPhaden (1999); the westward limb is largely outside the range of our analysis. We find relatively constant PV on the northern flank of the NSCC, but only weak to zero westward flow. The equatorward gyres, encompassed by our observations, include recirculation within the low-PV region, net input at the western boundary, and strong diapycnal flux divergences. There is a large mass flux input in the east and loss in the interior. In the Southern Hemisphere the circulation is more complicated because of the secondary SSCC, which has been omitted from the transport tables due to data paucity. Adding its transport to that of the primary SSCC would reduce the large difference between the NSCC and SSCC in the central and eastern regions, but would not eliminate it; the secondary SSCC is weak (Fig. 10). Particularly in the east, there is more westward return flow on the poleward flank of the SSCC and on both flanks of the secondary SSCC than on the poleward flank of the NSCC; but observations are few and the flows are weak. Nevertheless, we have included the westward flow between the SSCC and the secondary SSCC in Fig. 11.

A caution regarding temporal sampling is in order. Current variability on a broad range of time scales peaks at the equator, and the EIC is not always present; flow can be eastward on the equator from the EUC core down to more than 500 m (e.g., Firing 1987; see also Fig. 1 in Firing 1988). Because of the stringent data coverage requirements, Table 3 is based on seven sections in the west, of which none were during an El Niño; six sections in the central region, of which four were during the 1997–98 El Niño; and four sections in the east, of which one was during this event. The one El Niño section in the east has an EIC transport that is close to the mean

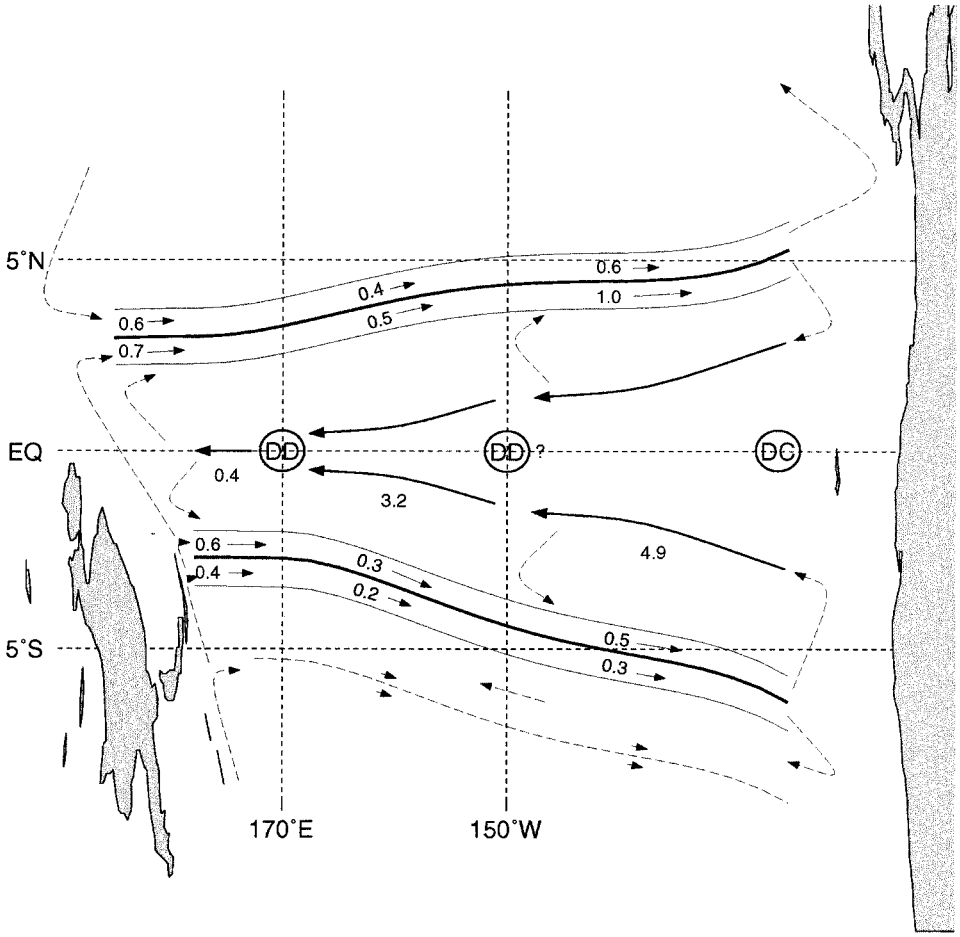

FIG. 11. Schematic circulation associated with the subsurface countercurrents. Numbers next to arrows give mean transports in the 26.5–26.6 kg m^{-3} neutral density layer (Table 3). The single number below each westward arrow south of the equator is the net transport between the NSCC and the SSCC on both sides of the equator, and including the eastward flow at the base of the equatorial undercurrent, where present. The NSCC and SSCC potential vorticity fronts are shown as heavy lines; the secondary SSCC front is the dashed line south of the SSCC. Dashed arrows show inferred recirculation paths, as well as the predominantly southern hemisphere source along the western boundary (Tsuchiya 1981). The encircled letters DD and DC indicate inferred diapycnal divergence (out of the layer) and convergence (into the layer), respectively, somewhere in the latitude band between the NSCC and SSCC fronts, not necessarily at the equator.

of the 4, however, so there is no evidence that the sample is badly biased. The main conclusions of the transport calculation, as summarized in Fig. 11, are based on the large excess of westward transport in the eastern region in contrast to the near balance of eastward and westward transports in the western region, so the El Niño sampling bias in the central region is not a major problem. The small number of samples overall, and particularly in the eastern region, does limit confidence in the mean transport calculations, and we plan to redo the averages as additional sections become available.

5. Discussion and conclusions

The description of the SCCs and adjacent flows based on velocity measurements and hydrography extends and modifies prior studies in two ways: first, it adds detail and geographical coverage; and second, it shifts attention from isopycnal to diapycnal processes in the regional circulation and dynamics.

The averaging of basinwide high-resolution SADCP measurements in stream coordinates shows the remarkable sharpness of the core velocity maximum and the corresponding sharpness of the PV front at the core. Increased PV gradient at the core was noted by the Gouriou and Toole (1993) study of velocity and hydrography in the western Pacific and by the Johnson and Moore (1997) and Johnson and McPhaden (1999) studies of basinwide hydrography, but the resolution was of order 1°; the present work shows that the meridional profile of zonal velocity is triangular at the core on at least the 10–20-km scale, and that the meridional

profile of PV consists of nearly constant PV pools extending well beyond the boundaries of the SCCs in both directions away from a front 40 km wide. The approximately step-function PV structure and the sharpness of the fronts have several implications. 1) An accurate numerical simulation of the SCCs will require higher resolution than present large-scale models have, although, as we have noted, it appears that high-resolution models are at least starting to develop SCCs (Ishida et al. 1998; Schott and Böning 1991). 2) The concept of the SCC cores as streamlines, or boundaries across which no advective mass or property fluxes occurs (Johnson and McPhaden 1999), is reinforced. 3) Lateral eddy fluxes across the fronts either must be very small or must be strongly counteracted by processes that maintain the sharpness of the fronts. 4) The system of adjacent zonally elongated gyres of which the SCCs are the eastward limbs may be driven to its step-function PV state as a limiting case. A small geostrophically adjusted increase in the strength of the gyres would cause reversals in the meridional derivative of PV, thereby satisfying a necessary condition for linear instability.

Extension of the traditional isopycnal framework for circulation studies in the SCCs (Tsuchiya 1981; Johnson and Moore 1997; Johnson and McPhaden 1999) to include a third dimension by applying continuity leads to the conclusion that diapycnal mass fluxes are an essential element of the regional mass balance; the diapycnal convergence into the central SCC layer, 26.5–26.6 kg m^{-3} in the east and out of it in the central and western regions involves diapycnal transports of the same magnitudes as the gyre recirculations themselves. The mass budget (Table 3) does not show where in latitude the diapycnal fluxes are occurring. It is conceivable, for example, that the diapycnal flux divergences occur primarily on the equator, in the base of the EUC and in the EIC. Downstream transport changes on isopycnals in the SCCs might then be balanced entirely by meridional isopycnal flux divergences. Even in this extreme case it is clear that the SCCs are not simple transport-conserving isopycnal pipes that cross the basin; meridional and/or diapycnal exchanges along the way are important.

As noted by Johnson and Moore (1997) and Johnson and McPhaden (1999), and as shown here in greater detail, the SCCs rise in depth and decrease in density as they flow from west to east. In the layer 26.3–26.5 kg m^{-3}, for example, there is relatively little SCC transport in the western and central regions but peak transport in the eastern region (Figs. 4 and 9); only a fraction of the water in the eastern SCCs in this layer can have arrived directly and isopycnally from the west. The SCCs seem to be more closely tied to the base of the thermocline than to a particular density range; they lighten to the east as the base of the thermocline lightens to the east with the development of the thermostad. For example, in Fig. 1 the base of the thermocline is at about 26.5 kg m^{-3} on 165°E versus 26–26.25 kg m^{-3} on 110°W. The coincidence of the top of the SCCs with the base of the thermocline is fundamental to the Johnson and Moore (1997) inertial theory, but, as they acknowledge, the downstream changes in SCC density and transport are not encompassed by the theory.

Both observationally and theoretically, many questions remain. We have said little here about SCC variability, for example, but plan to address it in detail as a natural extension of the present study. With respect to the mean circulation, there is good evidence for the general scheme in Fig. 11 with its six elongated gyres: proceeding from north to south, cyclonic and anticyclonic north of the equator, then anticyclonic, cyclonic, anticyclonic, and cyclonic south of the equator. The firmest parts of the picture are the SCCs, which form the boundaries between anticyclonic–cyclonic gyre pairs, although continuity of the secondary SSCC is unclear. The westward flows are hazier, and the meridional and diapycnal components are hazier still. The growing SADCP/CTD dataset from the TAO maintenance cruises will help, but dedicated float and microstructure observation programs may be required to pin down the meridional components and the diapycnal fluxes. On the theoretical side, we are still faced with the most basic questions about why the SCCs and their gyres exist at all and what are their sources and sinks of momentum and PV. Downstream changes in SCC properties, including PV on both sides of each front, indicate that the gyres are driven and dissipated at least partly in the basin interior rather than at the eastern and/or western boundaries alone. Like a western boundary gyre, the SCC gyres are isolated from the ocean surface, so they cannot be directly wind-driven; some combination of diapycnal fluxes and lateral eddy transfers must be responsible. As suggested by Gouriou and Toole (1993), the PV pool theory of Rhines and Young (1982) may be relevant.

Acknowledgments. This study was enabled by the Joint Archive for Shipboard ADCP, which provided a comprehensive equatorial Pacific SADCP dataset with references to the many field programs and investigators who contributed the hydrographic data. While the western Pacific was reasonably well sampled by the COARE and the US/PRC Cooperative Program for Air–Sea Interaction, the central and eastern Pacific have been the target of relatively few observational efforts including direct velocity measurements other than a few cruises completed in the early 1990s as part of the WOCE program. The value of the salinity, temperature, and velocity data collected on board the NOAA Ship *Ka'imimoana* during cruises primarily charged with servicing the TAO buoy network cannot be overstated. The *Ka'imimoana* data nearly tripled the number of realizations of the velocity and density field in the central and eastern Pacific—without it, this study would have been impossible or, at best, greatly diminished. We thank

the captain and crew of the *Ka'imimoana*, and in particular the survey technician, Dennis Sweeney.

The enthusiasm and insight of Dennis Moore stimulated this effort. Pat Caldwell assisted with the extraction of the SADCP datasets from the Joint Archive for SADCP. T. Delcroix, R. Lukas, P. Flament, H. Freeland, and many others provided data used in this study. J. Firing and K. McTaggart were largely responsible for the processing of the SADCP and CTD data, respectively, from the *Ka'imimoana.*

D. Rowe received financial support from the National Oceanic and Atmospheric Administration through Cooperative Agreement NA67RJ0154. E. Firing received financial support from the National Science Foundation Grant OCE97-30953. G. Johnson was supported by the NOAA Office of Oceanic and Atmospheric Research, the NOAA Climate and Global Change Program, and the NASA Physical Oceanography Program. The views expressed herein are those of the authors and do not necessarily reflect the view of NOAA or any of its subagencies.

REFERENCES

Delcroix, T., G. Eldin, and C. Hénin, 1987: Upper ocean water mases and transport in the western tropical Pacific (165°). *J. Phys. Oceanogr.,* **17,** 2248–2262.

Firing, E., 1987: Deep zonal currents in the central equatorial Pacific. *J. Mar. Res.,* **45,** 791–812.

——, 1988: Shallow equatorial jets. *J. Geophys. Res.,* **93,** 9213–9222.

Gouriou, Y., and J. Toole, 1993: Mean circulation of the upper layers of the western equatorial Pacific Ocean. *J. Geophys. Res.,* **98,** 22 495–22 520.

Hayes, S., J. Toole, and L. Mangum, 1983: Water-mass and transport variability at 110°W in the equatorial Pacific. *J. Phys. Oceanogr.,* **13,** 153–168.

Ishida, A., Y. Kashino, H. Mitsudera, N. Yoshioka, and T. Kadokura, 1998: Preliminary results of a global high-resolution GCM experiment. *J. Faculty Sci. Hokkaido Univ. Ser.,* **11 (2),** 441–469.

Jackett, D., and T. McDougall, 1997: A neutral density variable for the world's ocean. *J. Phys. Oceanogr.,* **27,** 237–263.

Johnson, G., and D. Moore, 1997: The Pacific equatorial subsurface countercurrents and an inertial model. *J. Phys. Oceanogr.,* **27,** 2448–2459.

——, and M. McPhaden, 1999: Interior pycnocline flow from the subtropical to the equatorial Pacific Ocean. *J. Phys. Oceanogr.,* **29,** 3073–3089.

King, B., and E. Cooper, 1993: Comparison of ship's heading determined from an array of gps antennas with heading from conventional gyrocompass measurements. *Deep-Sea Res.,* **40,** 2207–2216.

Mayer, D., R. Molinari, and J. Festa, 1998: The mean and annual cycle of upper layer temperature fields in relation to Sverdrup dynamics within the gyres of the Atlantic Ocean. *J. Geophys. Res.,* **103,** 18 545–18 566.

McPhaden, M., 1984: On the dynamics of equatorial subsurface countercurrents. *J. Phys. Oceanogr.,* **14,** 1216–1225.

——, and Coauthors, 1998: The Tropical Ocean-Global Atmosphere (TOGA) observing system: A decade of progress. *J. Geophys. Res.,* **103,** 14 169–14 240.

Rhines, P., and W. Young, 1982: Homogenization of potential vorticity in planetary gyres. *J. Fluid Mech.,* **122,** 347–367.

Schott, F., and C. Böning, 1991: The WOCE model in the western equatorial Atlantic: Upper layer circulation. *J. Geophys. Res.,* **96 (C4),** 6993–7004.

Toggweiler, J., K. Nixon, and W. Broecker, 1991: The Peru upwelling and the ventilation of the south Pacific thermocline. *J. Geophys. Res.,* **96,** 20 467–20 497.

Tsuchiya, M., 1975: Subsurface countercurrents in the eastern equatorial Pacific Ocean. *J. Mar. Res.,* **33** (Suppl.), 145–175.

——, 1981: The origin of the Pacific equatorial 13° water. *J. Phys. Oceanogr.,* **11,** 794–812.

——, 1986: Thermostads and circulation in the upper layer of the Atlantic Ocean. *Progress in Oceanography,* Vol. 16, Pergamon, 235–267.

Wyrtki, K., and B. Kilonsky, 1984: Mean water and current structure during the Hawaii-to-Tahiti shuttle experiment. *J. Phys. Oceanogr.,* **14,** 242–254.